

# Growth Kinetics and Size Distribution Dynamics of Viscous Secondary Organic Aerosol

Rahul A. Zaveri,<sup>\*,†</sup> John E. Shilling,<sup>†</sup> Alla Zelenyuk,<sup>‡</sup> Jiumeng Liu,<sup>†</sup> David M. Bell,<sup>‡,▽</sup> Emma L. D'Ambro,<sup>§,||</sup> Cassandra J. Gaston,<sup>§,◆</sup> Joel A. Thornton,<sup>§,||</sup> Alexander Laskin,<sup>⊥,◇</sup> Peng Lin,<sup>⊥,◇</sup> Jacqueline Wilson,<sup>‡</sup> Richard C. Easter,<sup>†</sup> Jian Wang,<sup>#</sup> Allan K. Bertram,<sup>¶</sup> Scot T. Martin,<sup>□,■</sup> John H. Seinfeld,<sup>○,●</sup> and Douglas R. Worsnop<sup>△</sup>

<sup>†</sup>Atmospheric Sciences and Global Change Division, Pacific Northwest National Laboratory, Richland, Washington 99352, United States

<sup>‡</sup>Physical Sciences Division, Pacific Northwest National Laboratory, Richland, Washington 99352, United States

<sup>§</sup>Department of Atmospheric Sciences, University of Washington, Seattle, Washington 98195, United States

<sup>||</sup>Department of Chemistry, University of Washington, Seattle, Washington 98195, United States

<sup>⊥</sup>William R. Wiley Environmental Molecular Sciences Laboratory, Pacific Northwest National Laboratory, Richland, Washington 99352, United States

<sup>#</sup>Environmental and Climate Sciences Department, Brookhaven National Laboratory, Upton, New York 11973, United States

<sup>¶</sup>Department of Chemistry, University of British Columbia, Vancouver, British Columbia V6T 1Z1, Canada

<sup>□</sup>John A. Paulson School of Engineering and Applied Sciences, Harvard University, Cambridge, Massachusetts 02138, United States

<sup>■</sup>Department of Earth and Planetary Sciences, Harvard University, Cambridge, Massachusetts 02138, United States

<sup>○</sup>Division of Chemistry and Chemical Engineering, California Institute of Technology, Pasadena, California 91125, United States

<sup>●</sup>Division of Engineering and Applied Science, California Institute of Technology, Pasadena, California 91125, United States

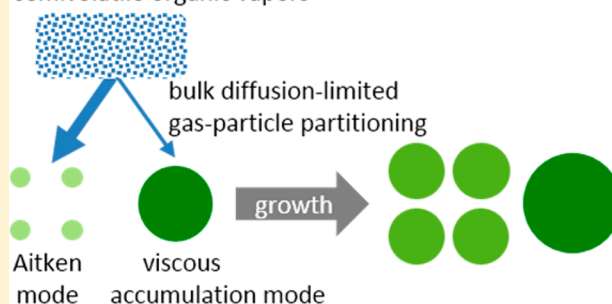
<sup>△</sup>Center for Aerosol and Cloud Chemistry, Aerodyne Research, Billerica, Massachusetts 01821, United States

## Supporting Information

**ABSTRACT:** Low bulk diffusivity inside viscous semisolid atmospheric secondary organic aerosol (SOA) can prolong equilibration time scale, but its broader impacts on aerosol growth and size distribution dynamics are poorly understood. Here, we present quantitative insights into the effects of bulk diffusivity on the growth and evaporation kinetics of SOA formed under dry conditions from photooxidation of isoprene in the presence of a bimodal aerosol consisting of Aitken (ammonium sulfate) and accumulation (isoprene or  $\alpha$ -pinene SOA) mode particles. Aerosol composition measurements and evaporation kinetics indicate that isoprene SOA is composed of several semivolatile organic compounds (SVOCs), with some reversibly reacting to form oligomers.

Model analysis shows that liquid-like bulk diffusivities can be used to fit the observed evaporation kinetics of accumulation mode particles but fail to explain the growth kinetics of bimodal aerosol by significantly under-predicting the evolution of the Aitken mode. In contrast, the semisolid scenario successfully reproduces both evaporation and growth kinetics, with the interpretation that hindered partitioning of SVOCs into large viscous particles effectively promotes the growth of smaller particles that have shorter diffusion time scales. This effect has important implications for the growth of atmospheric ultrafine particles to climatically active sizes.

semivolatile organic vapors



## INTRODUCTION

Secondary organic aerosol (SOA), produced by oxidation of anthropogenic and biogenic volatile organic compounds (VOC), constitutes a major fraction of the submicron atmospheric aerosol,<sup>1</sup> and plays a crucial role in the growth of nanoparticles to climatically active sizes of about 80 nm and higher.<sup>2–4</sup> The current understanding is that, in the absence of an appreciable particulate aqueous phase, SOA formation and particle growth

mechanisms depend strongly on the volatility (i.e., effective saturation vapor pressure,  $C^*$ ) of the oxidation products, and broadly fall into two categories: (1) kinetic condensation of

Received: September 7, 2017

Revised: December 4, 2017

Accepted: December 15, 2017

Published: December 15, 2017

extremely low-volatility compounds<sup>5</sup> ( $C^* < 3 \times 10^{-4} \mu\text{g m}^{-3}$ ) and supersaturated vapors to the pre-existing Fuchs-corrected surface area size distribution, facilitating the growth of the smallest particles,<sup>3,6</sup> and (2) Raoult's law-based equilibrium absorptive partitioning of semivolatile organic compounds (SVOC,  $0.3 < C^* < 300 \mu\text{g m}^{-3}$ ) to the pre-existing organic mass size distribution,<sup>7</sup> favoring the growth of larger particles.<sup>3,6</sup> The latter assumes that the absorbing particulate organic phase is liquid-like, implying rapid intraparticle diffusion of the condensing compounds (i.e., bulk diffusivity,  $D_b > 10^{-10} \text{cm}^2 \text{s}^{-1}$ ). Most atmospheric chemical transport models currently assume liquid organic particles with either rapid or instantaneous equilibration of SVOCs.<sup>8</sup> The use of the mass-based equilibrium versus the kinetic approach to partition all of the SOA formed in an atmospheric model can dramatically alter the aerosol size distribution and have a large impact on the simulated aerosol radiative effects.<sup>9</sup>

However, the physicochemical processes governing SOA formation are more complex than currently represented in atmospheric models.<sup>10</sup> For instance, SOA formation can occur via absorption of SVOCs into pre-existing aerosol, followed by rapid particle-phase reactions to form nonvolatile products.<sup>11,12</sup> A rapid particle-phase reaction effectively lowers the concentration of the condensing SVOC at the particle surface, and its effect is reflected in the evolution of the SOA size distribution.<sup>12,13</sup> In the case of an instantaneous particle-phase reaction, the surface concentration of the condensing compound becomes zero, and the resulting size distribution evolution is identical to that seen in kinetic condensation of nonvolatile compounds.<sup>14</sup> Relatively slower particle-phase accretion reactions of some SVOCs or "monomers" also produce significant amounts of effectively nonvolatile oligomers with large molecular weights.<sup>15–20</sup> These oligomers are thought to be responsible for increasing the viscosity of SOA particles, making them glassy or semisolid under dry to moderate relative humidity (RH), gradually transitioning to a liquid-like state at higher RH.<sup>19–27</sup> Low bulk diffusivity ( $D_b < 10^{-13} \text{cm}^2 \text{s}^{-1}$ ) inside viscous semisolid particles can slow down evaporation of SVOCs,<sup>28–31</sup> inhibit gas-particle partitioning of SVOCs, prolong equilibration time scales,<sup>14,32,33</sup> and affect chemical reactivity.<sup>34–37</sup> While increase in RH affects evaporation<sup>38–40</sup> and interparticle mixing processes<sup>41</sup> in some SOA systems, broader implications of low  $D_b$  on growth and size distribution dynamics of viscous SOA are poorly understood.

Here we report results from a laboratory chamber investigation of growth and evaporation kinetics of SOA formed from photooxidation of isoprene—the most abundantly emitted non-methane biogenic VOC on Earth.<sup>42</sup> Our experimental strategy consisted of a bimodal aerosol used as seeds upon which isoprene SOA was formed. SOA volatility was estimated from evaporation kinetics of size-selected particles at room temperature in a separate chamber.<sup>28,38</sup> The role of bulk diffusion in modulating gas-particle partitioning was then assessed through a model closure of the evaporation and growth kinetics, with compositional constraints provided by particle-phase organic speciation measurements.

## EXPERIMENTAL SECTION

**Growth Experiments.** Two aerosol growth kinetics experiments were conducted under dry (RH  $\approx$  10%) and low-NO<sub>x</sub> conditions in 10.6 m<sup>3</sup> FEP Teflon environmental chamber at Pacific Northwest National Laboratory<sup>43</sup> (Figure S1). The chamber was continually flushed with purified air prior to the start of each experiment until particle number concentrations  $< 10 \text{cm}^{-3}$  were observed with a Scanning Mobility Particle Sizer (SMPS).

The experiments were run in the batch mode where reactants were added to the chamber in discrete quantities.

Each experiment consisted of two stages. In stage 1 of experiment 1, isoprene was injected to the chamber either by evaporating a measured quantity of liquid under a stream of pure air or through addition of metered volumes from a calibrated cylinder. Hydrogen peroxide (50%, Aldrich) was evaporated into the chamber by gently warming the liquid under a flow of pure air and served as an OH radical precursor. Chamber RH was measured with a Rotronics sensor (SC-05) located inside the chamber. Aitken mode ammonium sulfate (AS) seed particles (dry diameter,  $D_p \approx 50 \text{nm}$ ) were injected into the chamber by atomizing, drying, and size-selecting them with a DMA (TSI, 3080L). Photochemistry was initiated by turning on 104 UV-blacklights (Q-laboratories, UV-340) symmetrically surrounding the chamber that produced a stable UV flux equivalent to a photolysis rate of  $J_{\text{NO}_2} = 0.2 \text{min}^{-1}$  and  $J_{\text{H}_2\text{O}_2} \approx 2.8 \times 10^{-3} \text{min}^{-1}$ . NO<sub>2</sub> photolysis rate was determined using two methods—the photochemical stationary state method<sup>44</sup> and by direct measurement using a  $J_{\text{NO}_2}$  radiometer.<sup>45</sup> The two measurements are in agreement. The H<sub>2</sub>O<sub>2</sub> photolysis rate was determined by tuning a simple model to generate the concentrations of OH needed to explain the observed isoprene decay rate. Multiple aliquots of the reactants were added and allowed to react to condense SOA on the AS seed particles and grow them to  $>200 \text{nm}$  (accumulation mode). The UV lights were then turned off and Aitken mode AS seed ( $D_p \approx 40 \text{nm}$ ) particles were then injected into the chamber to prepare the bimodal aerosol. Then in stage 2 of the experiment, the UV lights were turned on to form isoprene SOA on the pre-existing bimodal aerosol. At the end of stages 1 and 2, size-selected samples of the accumulation mode SOA particles, respectively, denoted as "P1" and "P2", were transferred into separate small chambers to study their evaporation kinetics under dry conditions (RH  $< 5\%$ ) and at room temperature.

Experiment 2 was conducted in same manner as experiment 1, except that the accumulation mode seed SOA (in stage 1) was formed from photooxidation of  $\alpha$ -pinene (instead of isoprene). The UV lights were turned off after  $\alpha$ -pinene was almost completely consumed toward the end of stage 1, followed by injection of isoprene and Aitken mode AS seed ( $D_p \approx 40 \text{nm}$ ) into the chamber. Then in stage 2, the UV lights were again turned on to form additional isoprene SOA on the pre-existing bimodal aerosol. The time evolution of key variables in experiments 1 and 2 are illustrated in Figures S2 and S3, respectively.

Isoprene and  $\alpha$ -pinene mixing ratio and some of their oxidation products were measured online (i.e., in real time) with a Proton Transfer Reaction Mass Spectrometer<sup>46</sup> (PTR-MS; Ionicon HS). The PTR-MS was regularly calibrated during the experimental work using a cylinder of known gas concentrations. Particle size distributions were measured continuously using an SMPS (TSI, 3936). The SMPS data were recorded with a time resolution of 5 min, and the instrument was set to measure particles in the range 14–710 nm mobility diameter divided into 110 logarithmically distributed size bins. Data were processed with standard TSI software including a correction for multiple-charged particles.

Aerosol composition was continuously measured with an Aerodyne High Resolution Time-of-Flight Aerosol Mass Spectrometer<sup>47,48</sup> (HR-ToF-AMS). AMS data were processed using standard techniques described in the literature and regularly calibrated through the laboratory campaign.<sup>49</sup> Volume measurements from the SMPS and that derived from the AMS

measurements agreed to within the measurement uncertainty. The SOA mass concentrations reported here were calculated from SMPS volume, using a density of  $1.4 \text{ g cm}^{-3}$  for SOA (measured by miniSPLAT) and  $1.77 \text{ g cm}^{-3}$  for the ammonium sulfate core.

A suite of oxygenated products in the particle-phase were analyzed in experiment 1 with a high-resolution time-of-flight chemical ionization mass spectrometer (HR-ToF-CIMS) using iodide adduct ionization as described previously,<sup>50–52</sup> coupled to a Filter Inlet for Gases and Aerosols<sup>51</sup> (FIGAERO). FIGAERO samples were timed to approximately coincide with the samples P1 and P2. After a particle collection period, the filter was heated at a rate of  $10$  or  $15 \text{ }^\circ\text{C min}^{-1}$  to  $200 \text{ }^\circ\text{C}$  for a temperature-programmed thermal desorption and then kept at  $200 \text{ }^\circ\text{C}$  for the remainder of the desorption time (40 min total desorption time). A more detailed description of FIGAERO and HR-ToF-CIMS is given in the [Supporting Information](#).

At the end of experiment 1, an aerosol sample taken from the environmental chamber was collected onto the Teflon filter for offline analysis. The SOA sample was probed directly from the filter using a custom-built Nanospray Desorption Electrospray Ionization (Nano-DESI) source coupled to a high resolution LTQ-Orbitrap mass spectrometer<sup>53,54</sup> (Thermo Electron, Bremen, Germany). A more detailed description of Nano-DESI-HRMS is given in the [Supporting Information](#).

**Evaporation Experiments.** The particle samples P1 and P2 (collected during experiment 1) were size-selected with a differential mobility analyzer (DMA, TSI Inc., Model 3081) and passed through two charcoal denuders (TSI Inc., Model 3062) connected in series and kept at room temperature to remove gas-phase organics. Particles with a narrow distribution of mobility diameters and low number concentrations ( $\sim 100 \text{ cm}^{-3}$ ) were loaded into one of the evaporation chambers (volumes of 7, 11, or 13 L) that were partially filled with activated charcoal to continuously remove the evaporated organics.<sup>28</sup> The evaporation chambers were operated at room temperature and  $\text{RH} < 5\%$ .

Typical duration of the evaporation experiments was  $\sim 24$  h during which particle vacuum aerodynamic diameter ( $D_{\text{va}}$ ), shape, density, and composition were periodically measured using single particle mass spectrometer, miniSPLAT<sup>55</sup> (a detailed description is given in the [Supporting Information](#)). Particle evaporation kinetics was thus quantified by measuring changes in  $D_{\text{va}}$  with 0.5% precision. Since the spherical SOA-containing particles did not change their shape during evaporation process, and the density of SOA increased only by  $< 2\%$  during early stages of evaporation and remained constant thereafter, the observed changes in  $D_{\text{va}}$  can be directly related to changes in volume fraction of organics, taking into account the contribution of AS seeds. While the particle number concentration in the evaporation chamber decreased because of wall losses and continual sampling, these losses had no effect on the evaporation rates, which were determined from the measured changes in particles  $D_{\text{va}}$ .

**Box Models.** A multilayer particle box model was used to interpret evaporation kinetics. The model divides a single spherical particle into 200 concentric layers and explicitly simulates mass transfer of multiple compounds from the particle by taking into account compound volatility ( $C^*$ ), gas-phase diffusivity ( $D_{\text{g}}$ ), interfacial mass accommodation ( $\alpha$ ), intraparticle bulk diffusivity ( $D_{\text{p}}$ ), and reversible particle-phase reactions.<sup>14</sup>

The sectional aerosol box model MOSAIC (Model for Simulating Aerosol Interactions and Chemistry)<sup>14,56</sup> was used to interpret the observed bimodal aerosol growth kinetics. MOSAIC dynamically partitions multiple compounds to all

particle size bins by taking into account compound volatility, gas-phase diffusion, interfacial mass accommodation, intraparticle bulk diffusion, and reversible particle-phase reactions. The thermodynamic driving force for mass transfer is governed by Raoult's law; bulk diffusion is treated using the two-film theory. More detailed descriptions of the multilayer model and MOSAIC are given in the [Supporting Information](#).

## RESULTS AND DISCUSSION

**Figure 1** shows the observed time evolutions of aerosol number and volume size distributions to illustrate the growth kinetics of the bimodal aerosol due to isoprene SOA formation during stage 2 of experiments 1 and 2. In terms of mode diameters, the  $\sim 40$  nm Aitken mode rapidly grew to about 100 nm or more while the accumulation mode experienced relatively modest growth. **Table S1** summarizes the mode diameters and SOA mass concentrations in the two modes at the beginning of stage 1 (initial) and after  $\Delta t = 60$  (experiment 1) and 32 min (experiment 2) of growth. Our objective is to unravel the physicochemical mechanisms governing the growth kinetics of the two modes in both experiments.

Multigenerational photooxidation of isoprene forms many products, but their yields, volatilities, and SOA formation mechanisms are uncertain. Under dry and low- $\text{NO}_x$  conditions, as is the case here, isoprene photooxidation can form isoprene dihydroxydihydroperoxide ( $\text{C}_5\text{H}_{12}\text{O}_6$ ) and related species that lead to SOA formation.<sup>45,52,57</sup> Since growth kinetics crucially depends on the volatility of the condensing compounds, as well as their particle-phase diffusivity and reactivity,<sup>12,14</sup> we first interpreted the evaporation kinetics to estimate these quantities, and then used them to constrain the interpretation of the growth kinetics.

**Interpreting Evaporation Kinetics.** A multilayer particle model was used to simulate the evaporation of size-selected accumulation mode isoprene SOA samples P1 (initial) and P2 (after growth) obtained in experiment 1. FIGAERO thermograms showed that about 50–60% of isoprene SOA mass was composed of  $\text{C}_5\text{H}_{12}\text{O}_5$  and  $\text{C}_5\text{H}_{12}\text{O}_6$  while the remaining 40–50% mass consisted of several compounds that desorbed at unexpectedly high temperatures and were inferred as thermal fragmentation products of oligomers<sup>52</sup> (**Figure 2a** and **2b**). The total SOA mass estimated from the sum of individual FIGAERO thermograms was in excellent agreement (within  $\sim 4\%$  difference) with that calculated using SMPS volume. Additionally, offline Nano-DESI-HRMS analysis of isoprene SOA sample qualitatively confirmed the presence of  $\text{C}_5\text{H}_{12}\text{O}_5$  and  $\text{C}_5\text{H}_{12}\text{O}_6$  as major products mixed with several different oligomers (**Figure 2c**). The particle-phase O:C ratio for isoprene SOA, as determined from the HR-ToF-AMS measurements, remained at  $\sim 0.9$  throughout Stages 1 and 2.

The compositions of SOA samples P1 and P2 are summarized in **Figure 3a**. As shown in **Figures 3c** and **3d**, more than 90% of isoprene SOA evaporated over a period of about 25–28 h. This suggests that the oligomers slowly decomposed at room temperature to form semivolatile monomers that subsequently evaporated from the particles.<sup>58</sup> Furthermore, the distinctly different rates of evaporation over the first 5 h and the subsequent 15–20 h periods suggest the presence of at least two types of oligomers with different decomposition time scales. The complex mixture of oligomers was represented in the model by two surrogate nonvolatile dimers,  $\text{Dimer}_1$  and  $\text{Dimer}_2$ , each reversibly formed from respective surrogate monomers,  $\text{SVOC}_1$

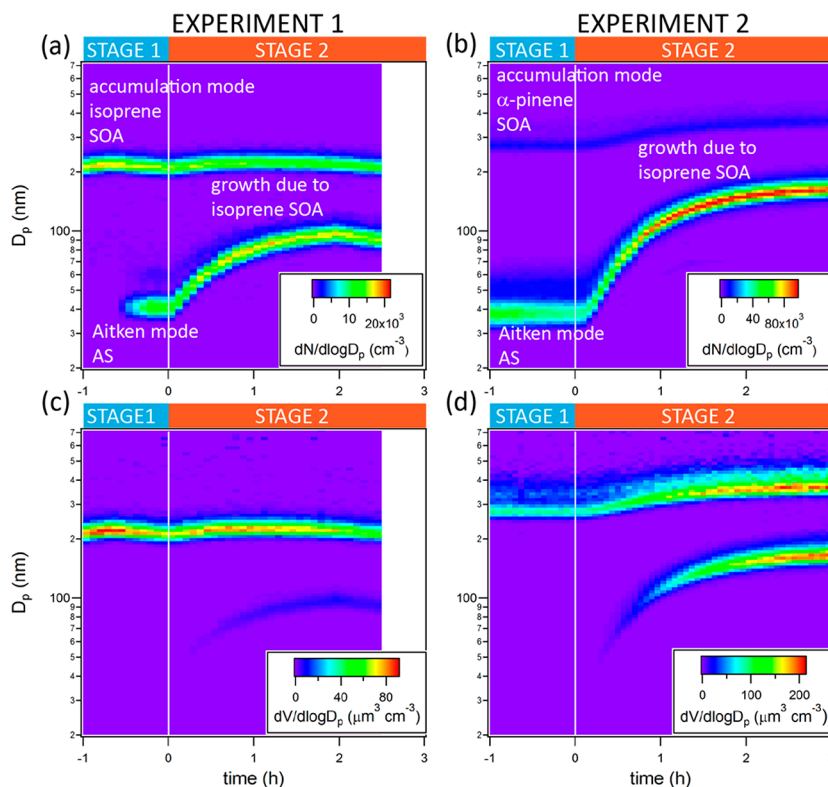
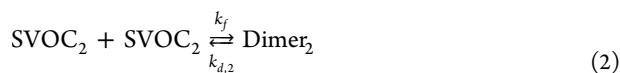
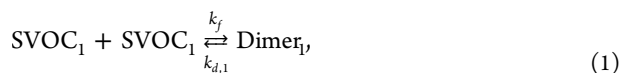


**Figure 1.** Observed time evolutions of (a, b) aerosol number size distributions and (c, d) aerosol volume size distributions in experiments 1 and 2. The initial (end of stage 1) bimodal aerosol in experiment 1 consists of an Aitken mode composed of ammonium sulfate (AS) and an accumulation mode composed of isoprene SOA. The initial (end of stage 1) bimodal aerosol in experiment 2 consists of an Aitken mode composed of AS and an accumulation mode composed of  $\alpha$ -pinene SOA. Growth of the bimodal aerosol in stage 2 occurred because of isoprene SOA formation in both experiments.

and  $\text{SVOC}_2$ , with the same formation rate constant ( $k_f$ ) but different decomposition constants ( $k_{d,1}$  and  $k_{d,2}$ ):



Since evaporating monomers could not be explicitly identified from FIGAERO thermograms, both  $\text{SVOC}_1$  and  $\text{SVOC}_2$  were assumed to have molecular weights of  $136 \text{ g mol}^{-1}$  and their corresponding dimers were assumed to have molecular weights of  $272 \text{ g mol}^{-1}$ . The dimer–monomer pairs were assumed to be at equilibrium and uniformly distributed in the particle’s organic phase at the start of the evaporation experiment. Mass accommodation coefficients ( $\alpha$ ) of all the evaporating compounds were assumed at 0.1. The bulk gas-phase concentrations were assumed at zero as the particle evaporated.

The multilayer model was manually iterated to determine the volatility ( $C^*$ ) of the four compounds ( $\text{C}_5\text{H}_{12}\text{O}_5$ ,  $\text{C}_5\text{H}_{12}\text{O}_6$ ,  $\text{SVOC}_1$ ,  $\text{SVOC}_2$ ) for different values of  $D_b$ ,  $k_f$ ,  $k_{d,1}$ , and  $k_{d,2}$  that reproduced the observed evaporation kinetics. Although this problem has multiple solutions due to lack of enough independent constraints, the plausible solutions (i.e., those that take into account reversible oligomer formation) required all four evaporating species to be semivolatile (i.e.,  $C^* > 0.3 \mu\text{g m}^{-3}$ ). A set of rate constants values of  $k_f = 3 \times 10^{-6} \text{ m}^3 \text{ mol}^{-1} \text{ s}^{-1}$ ,  $k_{d,1} = 5 \times 10^{-4} \text{ s}^{-1}$ , and  $k_{d,2} = 1.4 \times 10^{-5} \text{ s}^{-1}$  was determined such that the pseudo-first order forward reaction time scales of  $\text{SVOC}_1$  and  $\text{SVOC}_2$  at equilibrium were respectively about 10 and 30 min. The room temperature decomposition time scales of  $\text{Dimer}_1$  and

$\text{Dimer}_2$  were respectively about 30 and 1000 min, such that the dimers constituted the dominant fraction at equilibrium. Upon heating the SOA samples at the rate of  $10\text{--}15 \text{ }^\circ\text{C min}^{-1}$  to  $200 \text{ }^\circ\text{C}$ , FIGAERO detected small, high volatility compounds during desorption, suggesting they are likely fragmentation products of oligomers<sup>59–61</sup> as opposed to decomposition of oligomers to monomers. The FIGAERO thermograms support the long decomposition time scales estimated here for the two dimers, such that they would largely fragment before decomposing back to monomers during temperature-programmed thermal desorption. Using the same set of values for the rate constants, it was possible to obtain different sets of  $C^*$  values as a function of  $D_b$  that reproduced the observed evaporation kinetics. The same value of  $D_b$  was assumed for all four compounds and was held constant throughout the simulation.

Figure 3b shows two sets of  $C^*$  values for: (i) high bulk diffusivity values representing the “liquid-like scenario” ( $D_b > 10^{-10} \text{ cm}^2 \text{ s}^{-1}$ ), and (ii) a low bulk diffusivity value representing the “semisolid scenario” ( $D_b = 2 \times 10^{-15} \text{ cm}^2 \text{ s}^{-1}$ ). The  $D_b$  value in semisolid scenario is consistent with the low end of the range recently estimated for isoprene SOA under dry conditions, based on the Stokes–Einstein relation between viscosity and diffusivity.<sup>25</sup> In both scenarios, the  $C^*$  of  $\text{C}_5\text{H}_{12}\text{O}_5$  and  $\text{C}_5\text{H}_{12}\text{O}_6$  were  $\sim 1\text{--}2 \mu\text{g m}^{-3}$ , consistent with the  $0.5\text{--}2 \mu\text{g m}^{-3}$  range independently estimated from FIGAERO thermograms.<sup>52</sup> The  $C^*$  of  $\text{SVOC}_1$  and  $\text{SVOC}_2$  were 30 and  $3 \mu\text{g m}^{-3}$  in the liquid-like scenario, while they were both  $30 \mu\text{g m}^{-3}$  in the semisolid scenario. The predicted evaporation curves for the liquid-like and semisolid scenarios are shown in Figures 3c and 3d, respectively. The evaporation profiles of individual compounds are shown in Figure S4. Similar sets of  $C^*$  values can be obtained

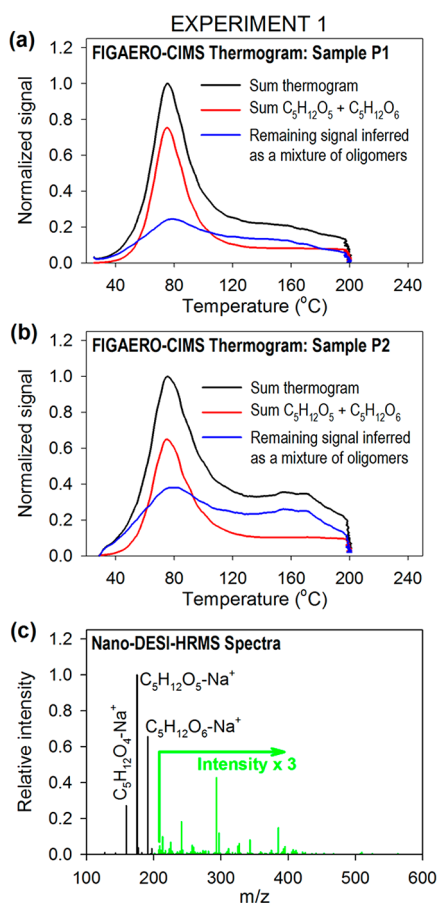


**Figure 2.** Chemical composition of isoprene SOA formed in experiment 1. (a) FIGAERO HR-ToF-CIMS thermograms for sample P1. The sum thermogram (black line) represents the sum signal of all compounds with formula  $C_xH_yO_zI$ . The remainder of the signal is shown in blue. While the sum of  $C_5H_{12}O_5$  and  $C_5H_{12}O_6$  (red line) have a Gaussian-like shape with a defined  $T_{max}$  at 75–78 °C, the remaining signal (blue line) shows a broad desorption profile. The thermogram of the remaining signal shows that the material is resistant to evaporation and is inferred as a mixture of oligomers. (b) FIGAERO HR-ToF-CIMS thermograms for sample P2. (c) Nano-DESI-HRMS spectra of SOA sample collected at the end of the experiment, with the positive mode ions identified and assigned with  $C_xH_yO_z$  formulas.

by varying  $D_b$ ,  $k_f$ ,  $k_{d,1}$ , and  $k_{d,2}$ . In general, the fitted  $C^*$  values of all compounds tended to increase (or remained constant) with decreasing  $D_b$ . The fitted  $C^*$  values of  $C_5H_{12}O_5$  and  $C_5H_{12}O_6$  were insensitive to variation in  $k_f$ ,  $k_{d,1}$ , and  $k_{d,2}$  while the fitted  $C^*$  values of  $SVOC_1$  and  $SVOC_2$  decreased with increasing values of these rate constants. It was also possible to reproduce evaporation kinetics by ignoring oligomer formation and instead simply assuming that the evaporating compounds do not chemically react within liquid-like particles. In this scenario (not shown in Figure 3), the fitted  $C^*$  values for  $C_5H_{12}O_5$ ,  $C_5H_{12}O_6$ ,  $SVOC_1$ , and  $SVOC_2$  were 1.1, 1.1, 10, 0.05  $\mu\text{g m}^{-3}$ , respectively. Here,  $SVOC_2$  is a low volatility compound instead of semivolatile, and this scenario is referred to as “low-volatility scenario”.

The question is which, if any, of these estimated sets of  $C^*$  and  $D_b^*$  values can also explain the observed growth kinetics, with the implicit assumption that the compounds inferred from evaporation kinetics are the same as those that condensed from the gas phase to form the SOA.

**Interpreting Growth Kinetics.** Figure 4 shows the growth of the bimodal aerosol during stage 2 of experiment 1. Over a

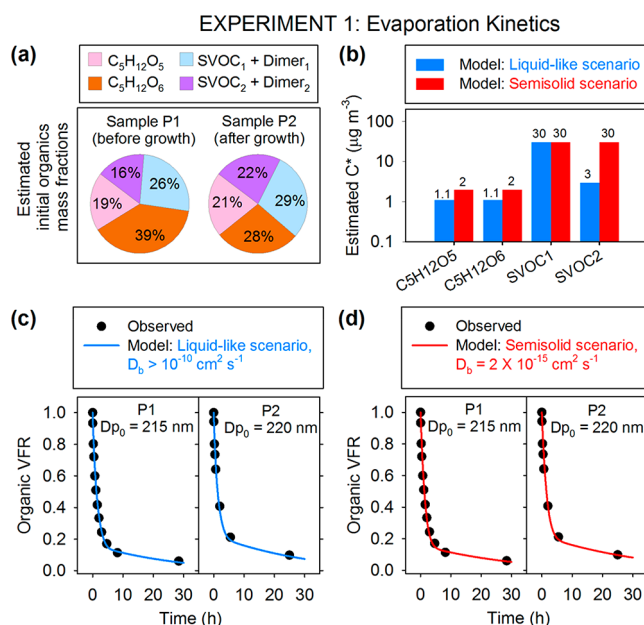


**Figure 3.** Evaporation kinetics of the accumulation mode isoprene SOA particles obtained in experiment 1. (a) Estimated initial compositions of SOA in samples P1 and P2 (as indicated in Figure S2a) based on interpretation of FIGAERO–CIMS thermograms (Figure 2a). Sample P1 represents aged isoprene SOA formed during stage 1 of the experiment and sample P2 represents its state after additional isoprene SOA formation in stage 2. (b) Estimated volatilities ( $C^*$ ) of the four constituent compounds, with SOA modeled as liquid-like (with  $D_b > 10^{-10} \text{ cm}^2 \text{ s}^{-1}$ ) and as semisolid (with  $D_b = 2 \times 10^{-15} \text{ cm}^2 \text{ s}^{-1}$ ). Comparison of the observed organic volume fraction remaining (VFR) as a function of time for the P1 and P2 samples with that modeled as (c) liquid-like and (d) semi-solid. The model was initialized using the estimated SOA compositions shown in panel a and the estimated species volatilities shown in panel b.

period of 60 min, the  $\sim 40$  nm Aitken mode grew to 82 nm, while the 209 nm accumulation mode grew to 217 nm. In terms of the newly added SOA mass, the Aitken and accumulation modes grew by 0.45 and 1.48  $\mu\text{g m}^{-3}$ , respectively, after correcting for particle wall loss. We used the sectional aerosol box-model MOSAIC to simulate the effects of volatility and bulk diffusivity on the growth kinetics of these two modes. Isoprene mixing ratio and aerosol size distribution in the model were initialized using observations at the beginning of stage 2. The compositions of the Aitken and accumulation modes were initialized to ammonium sulfate and that estimated for the P1 sample (with a 50 nm ammonium sulfate core), respectively. The OH radical concentration in the model was tuned to reproduce the observed decay of isoprene in the chamber. Although it takes several steps to produce condensable oxidation products from isoprene photo-oxidation, the isoprene + OH reaction in the model was parametrized to directly form  $C_5H_{12}O_5$ ,  $C_5H_{12}O_6$ ,  $SVOC_1$ , and  $SVOC_2$ . The gas-phase yields of these four compounds were then adjusted such that the final bulk SOA composition predicted by the model matched that of the P2 sample, while the total amount of SOA formed in the model was constrained to the wall-loss corrected value of 1.93  $\mu\text{g m}^{-3}$  observed after 60 min. This modeling approach effectively circumvents the uncertainties associated with gas-phase multigenerational photochemistry of isoprene and the yields of condensable oxidation products, their volatilities, and vapor wall losses. The simulation period ( $\Delta t$ ) was limited to 60 min so that particle wall loss could be neglected in the model calculations.

The two sets of  $C^*$  values shown in Figure 3b were used to simulate the growth kinetics for the liquid-like and semisolid scenarios. And as done previously, the same set of values for  $k_p$ ,  $k_{d,1}$ , and  $k_{d,2}$  was used for both scenarios. In the liquid-like scenario, the growth predictions were essentially insensitive to  $D_b > 10^{-10} \text{ cm}^2 \text{ s}^{-1}$ . In the semisolid scenario, the Aitken and accumulation modes were allowed to take different values of  $D_b$ , but the prescribed value in each mode was held constant throughout the simulation for simplicity. We did not attempt to parametrize  $D_b$  as a function of composition in this study due to the large uncertainty associated with this parameter. Finally, we also simulated the growth kinetics by assuming that SOA was entirely formed from condensation of a single nonvolatile vapor. This scenario, which is referred to as the “nonvolatile scenario,” represents the extreme version of the low-volatility scenario discussed in the Interpreting Evaporation Kinetics section. Two simulations were carried out with mass accommodation coefficient value for the nonvolatile vapor of  $\alpha = 0.1$  and  $\alpha = 1$ . Although clearly implausible in the light of the evaporation data, the two nonvolatile scenarios examine the extreme sensitivity of the predicted aerosol growth kinetics to the volatility and mass accommodation coefficient of the condensing vapor. Lastly, aerosol growth kinetics due to instantaneous particle-phase chemical reaction of a semivolatile vapor is identical to that from condensation of a nonvolatile vapor. Thus, the nonvolatile scenarios also examine the extreme sensitivity of the predicted growth kinetics to the rate constant of the reactive semivolatile vapors that form oligomers.

Figure 4 shows that the liquid-like scenario appears to reproduce the size of the accumulation mode particles, but severely

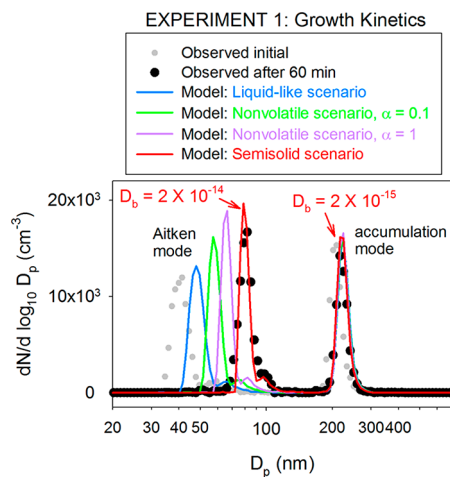


**Figure 4.** Comparison of the observed and predicted aerosol size distribution evolution due to isoprene SOA formation during stage 2 of experiment 1. Gray dots represent the observed initial bimodal aerosol size distributions consisting of Aitken mode ammonium sulfate particles and accumulation mode isoprene SOA. Black dots represent the observed size distribution after growth due to additional isoprene SOA formation. The lines represent model predictions for different scenarios. The liquid-like scenario (with  $D_b > 10^{-10} \text{ cm}^2 \text{ s}^{-1}$ ) assumes rapid diffusion of the condensing organic molecules inside the particle phase—similar to instantaneous equilibrium gas-particle partitioning—and grossly under predicts the growth of the Aitken mode. Even the nonvolatile vapor condensation scenarios, with mass accommodation coefficient  $\alpha = 0.1$  and 1, fail to explain the growth of the Aitken mode. The semisolid scenario successfully reproduces the growth of both the Aitken and accumulation modes, with the required  $D_b$  values as indicated in the plot.

under-predicted the growth of the Aitken mode. By neglecting bulk diffusion limitation, the liquid-like scenario tends to partition the condensing semivolatile organic vapors according to the pre-existing organic mass size distribution. As a result, the liquid-like scenario partitioned  $1.89 \mu\text{g m}^{-3}$  (instead of observed  $1.48 \mu\text{g m}^{-3}$ ) of the newly formed SOA to the accumulation mode at the expense of the Aitken mode, which received just  $0.04 \mu\text{g m}^{-3}$  (instead of the observed  $0.45 \mu\text{g m}^{-3}$ ). The non-volatile scenarios with  $\alpha = 0.1$  and  $\alpha = 1$  were progressively better than the liquid-like scenario with respect to the predicted growth of the Aitken mode, but still fell significantly short compared to the observed growth. A nonvolatile vapor or a highly reactive semivolatile vapor condenses according to the pre-existing Fuchs-corrected surface area size distribution and thereby favors the growth of the smallest particles. Thus, the nonvolatile scenario with  $\alpha = 1$  represents the maximum possible growth of the Aitken mode within the conventional modeling framework, but it still failed to explain the observations.

In contrast to the liquid-like and nonvolatile scenarios, the semisolid scenario was able to reproduce the growths of both Aitken and accumulation modes when their  $D_b$  values were set to  $2 \times 10^{-14}$  and  $2 \times 10^{-15} \text{ cm}^2 \text{ s}^{-1}$ , respectively, with the latter being identical to that needed to reproduce the evaporation kinetics of the accumulation mode SOA. An order of magnitude larger value of  $D_b$  required for the Aitken mode appears to be consistent with the relatively less volatile  $\text{C}_5\text{H}_{12}\text{O}_3$  and  $\text{C}_5\text{H}_{12}\text{O}_6$  initiating a liquid-like organic phase in the Aitken mode that then facilitated the absorption of more volatile vapors, which subsequently formed oligomers and gradually increased the viscosity with aging.<sup>28,30,62</sup> In contrast, the pre-existing SOA in the accumulation mode was relatively more aged, and hence more viscous, less volatile, and less diffusive. The resulting hindered growth of the accumulation mode SOA thus promoted the growth of the Aitken mode particles that were able to compete more effectively for the condensing semivolatile vapors. Figure S5 illustrates the sensitivity of the predicted growth kinetics to the prescribed  $D_b$  values for each mode in experiment 1, with the semisolid scenario  $D_b$  values shown in Figure 4 as the base case. It can be seen that a higher than base case  $D_b$  value for the accumulation mode or a lower than base case  $D_b$  value for the Aitken mode appreciably slows down the growth of the Aitken mode. In contrast, a lower than base case  $D_b$  for the accumulation mode over predicts the growth of the Aitken mode.

Similar results were obtained for experiment 2 in which isoprene SOA was formed in the presence of Aitken mode ammonium sulfate and accumulation mode  $\alpha$ -pinene SOA seed particles. While  $\alpha$ -pinene SOA is expected to be composed of a mixture of several compounds and oligomers, it was assumed in the model to be composed of a nonvolatile surrogate compound with a molecular weight of  $200 \text{ g mol}^{-1}$  for the purpose of kinetically partitioning isoprene SOA into it as governed by Raoult's law. As before, the isoprene mixing ratio and aerosol size distribution in the model were initialized using observations at the beginning of stage 2. The same two sets  $C^*$  values for the liquid-like and semisolid scenarios along with the same set of values for  $k_p$ ,  $k_{d,1}$ , and  $k_{d,2}$  were used as previously employed for modeling experiment 1. Because of the lack of FIGAERO-CIMS speciation measurements in experiment 2, the gas-phase yields of the four condensing compounds were adjusted to match the bulk composition of sample P2 of experiment 1 (shown in Figure 3a). The total amount of predicted isoprene SOA was constrained to the wall-loss corrected observed value of  $4.53 \mu\text{g m}^{-3}$  after 32 min into stage 2 of experiment 2. As shown in Figure 5, the liquid-like

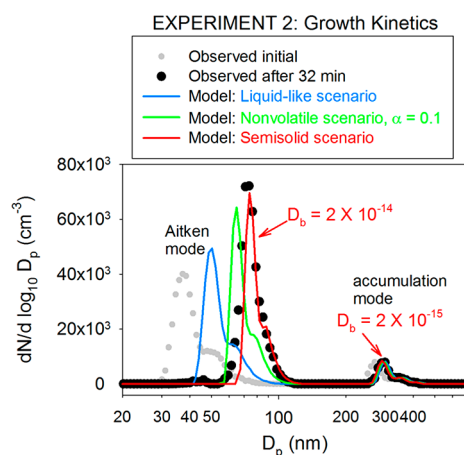


**Figure 5.** Comparison of the observed and predicted aerosol size distribution evolution due to isoprene SOA formation during stage 2 of experiment 2. Gray dots represent the observed initial bimodal aerosol size distributions consisting of Aitken mode ammonium sulfate particles and accumulation mode  $\alpha$ -pinene SOA. Black dots represent the observed size distribution after growth due to additional isoprene SOA formation. The lines represent model predictions for different scenarios. The liquid-like ( $D_b > 10^{-10} \text{ cm}^2 \text{ s}^{-1}$ ) and nonvolatile ( $\alpha = 0.1$ ) scenarios under-predict the growth of the Aitken mode while the semisolid scenario successfully reproduces the growth of both the Aitken and accumulation modes, with the required  $D_b$  values as indicated in the plot.

and nonvolatile scenarios again under-predicted the growth of the Aitken mode while the semisolid scenario was able to capture the growths of both the Aitken and accumulation modes when their  $D_b$  values were respectively set to  $2 \times 10^{-14}$  and  $2 \times 10^{-15} \text{ cm}^2 \text{ s}^{-1}$ —the same as those used in modeling experiment 1. In general,  $\alpha$ -pinene SOA is expected to be more viscous than isoprene SOA.<sup>25</sup> However, large uncertainty exists in the viscosity measurements for  $\alpha$ -pinene SOA under dry conditions,<sup>25</sup> with additional uncertainty present in estimating  $D_b$  values using Stokes–Einstein relationship. The identical  $D_b$  values for isoprene and  $\alpha$ -pinene SOA needed in the present calculations is therefore likely fortuitous, but nevertheless affirm the presence of appreciable particle-phase diffusion limitation in the aged accumulation mode SOA in both experiments. Figure S6 illustrates the sensitivity of the predicted growth kinetics to the prescribed  $D_b$  values for each mode in experiment 2, with the semisolid scenario  $D_b$  values shown in Figure 5 as the base case. The sensitivity results are similar to those discussed for experiment 1.

Since any particle-phase diffusion limitation to condensing SVOCs should inhibit the growth of both small and large particles, the enhanced growth of small particles resulting from diffusion-limited growth may therefore seem counterintuitive. However, this is possible because the intraparticle bulk diffusion time scales varies as  $D_p^2$ , while the particle mass varies as  $D_p^3$ . For instance, organic particles with  $D_p = 20$  and 200 nm, respectively, have bulk diffusion time scales of about 1 and 100 min for the same value of  $D_b = 1 \times 10^{-15} \text{ cm}^2 \text{ s}^{-1}$ , but the amount of mass needed to double the size of one hundred 20 nm particles is equivalent to growing a single 200 nm particle to 240 nm. Therefore, even modest hindrance in the uptake of SVOCs by large semisolid particles allows the SVOCs to be available for absorption by ultrafine particles that have shorter diffusion time scales due to smaller size. If these SVOCs undergo particle-phase reactions to form low volatility products, as is the case in the present study, then the small particles will continue to absorb the SVOCs and grow at the expense of larger particles. Although

growth kinetics experiments need to be conducted as a function of RH and for other SOA systems, current results demonstrate that hindered growth of large viscous organic particles in the atmosphere can enhance the growth of coexisting ultrafine particles and thereby affect the production of climatically active particles under relatively dry conditions in the midlatitudes, as well as under relatively cold conditions in the middle and upper troposphere where organic particles likely exist in semisolid or solid-phase state.<sup>62</sup>

## ■ ASSOCIATED CONTENT

### Supporting Information

The Supporting Information is available free of charge on the ACS Publications website at DOI: 10.1021/acs.est.7b04623.

Detailed information on mass spectrometers and box models; summary of aerosol growth experiments; time evolution of key variables in aerosol growth experiments; evaporation profiles of total particle and individual compounds; and sensitivity of growth kinetics to the prescribed bulk diffusivity values for the Aitken and accumulation modes in aerosol growth experiments (PDF)

## ■ AUTHOR INFORMATION

### Corresponding Author

\*Phone: 206-528-3215. E-mail: rahul.zaveri@pnnl.gov.

### ORCID

Rahul A. Zaveri: 0000-0001-9874-8807

Emma L. D'Ambro: 0000-0002-3041-9027

Joel A. Thornton: 0000-0002-5098-4867

Alexander Laskin: 0000-0002-7836-8417

### Present Addresses

▽ Laboratory of Atmospheric Chemistry, Paul Scherrer Institute, 5232 Villigen-PSI, Switzerland.

◆ Rosenstiel School of Marine & Atmospheric Science, University of Miami, Miami, FL 33149, USA.

◇ Department of Chemistry, Purdue University, West Lafayette, IN 47907, USA.

### Notes

The authors declare no competing financial interest.

## ■ ACKNOWLEDGMENTS

This research was supported by the Office of Science of the U.S. Department of Energy (DOE) as part of the Atmospheric System Research program and by the Environmental Molecular Sciences Laboratory, a national scientific user facility sponsored by the DOE's Office of Biological and Environmental Research at Pacific Northwest National Laboratory (PNNL). PNNL is operated for DOE by Battelle Memorial Institute under contract DE-AC05-76RL01830. Data used in this work are available from the corresponding author (rahul.zaveri@pnnl.gov).

## ■ REFERENCES

- Zhang, Q.; Jimenez, J. L.; Canagaratna, M. R.; Allan, J. D.; Coe, H.; Ulbrich, I.; Alfarra, M. R.; Takami, A.; Middlebrook, A. M.; Sun, Y. L.; Dzepina, K.; Dunlea, E.; Docherty, K.; De-Carlo, P. F.; Salcedo, D.; Onasch, T.; Jayne, J. T.; Miyoshi, T.; Shimojo, A.; Hatakeyama, S.; Takegawa, N.; Kondo, Y.; Schneider, J.; Drewnick, F.; Borrmann, S.; Weimer, S.; Demerjian, K.; Williams, P.; Bower, K.; Bahreini, R.; Cottrell, L.; Griffin, R. J.; Rautiainen, J.; Sun, J. Y.; Zhang, Y. M.; Worsnop, D. R. Ubiquity and dominance of oxygenated species in organic aerosols in anthropogenically-influenced Northern Hemisphere mid-latitudes. *Geophys. Res. Lett.* **2007**, *34*, L13801.

- (2) Pierce, J. R.; Leitch, W. R.; Liggio, J.; Westervelt, D. M.; Wainwright, C. D.; Abbatt, J. P. D.; Ahlm, L.; Al-Basheer, W.; Cziczo, D. J.; Hayden, K. L.; Lee, A. K. Y.; Li, S.-M.; Russell, L. M.; Sjöstedt, S. J.; Strawbridge, K. B.; Travis, M.; Vlasenko, A.; Wentzell, J. J. B.; Wiebe, H. A.; Wong, J. P. S.; Macdonald, A. M. Nucleation and condensational growth to CCN sizes during a sustained pristine biogenic SOA event in a forested mountain valley. *Atmos. Chem. Phys.* **2012**, *12*, 3147–3163.
- (3) Riipinen, I.; Pierce, J. R.; Yli-Juuti, T.; Nieminen, T.; Häkkinen, S.; Ehn, M.; Junninen, H.; Lehtipalo, K.; Petäjä, T.; Slowik, J.; Chang, R.; Shantz, N. C.; Abbatt, J.; Leitch, W. R.; Kerminen, V.-M.; Worsnop, D. R.; Pandis, S. N.; Donahue, N. M.; Kulmala, M. Organic condensation: a vital link connecting aerosol formation to cloud condensation nuclei (CCN) concentrations. *Atmos. Chem. Phys.* **2011**, *11*, 3865–3878.
- (4) Riipinen, I.; Yli-Juuti, T.; Pierce, J. R.; Petäjä, T.; Worsnop, D. R.; Kulmala, M.; Donahue, N. M. The contribution of organics to atmospheric nanoparticle growth. *Nat. Geosci.* **2012**, *5*, 453–458.
- (5) Jokinen, T.; Berndt, T.; Makkonen, R.; Kerminen, V.-M.; Junninen, H.; Paasonen, P.; Stratmann, F.; Herrmann, H.; Guenther, A.; Worsnop, D. R.; Kulmala, M.; Ehn, M.; Sipilä, M. Production of extremely low-volatile organic compounds from biogenic emissions: measured yields and atmospheric implications. *Proc. Natl. Acad. Sci. U. S. A.* **2015**, *112*, 7123–7128.
- (6) Zhang, Xi; Pandis, S. N.; Seinfeld, J. H. Diffusion-limited versus quasi-equilibrium aerosol growth. *Aerosol Sci. Technol.* **2012**, *46*, 874–885.
- (7) Pankow, J. F. An absorption model of gas/particle partitioning of organic compounds in the atmosphere. *Atmos. Environ.* **1994**, *28*, 185–188.
- (8) Tsigaridis, K.; Daskalakis, N.; Kanakidou, M.; Adams, P. J.; Artaxo, P.; Bahadur, R.; Balkanski, Y.; Bauer, S. E.; Bellouin, N.; Benedetti, A.; Bergman, T.; Berntsen, T. K.; Beukes, J. P.; Bian, H.; Carslaw, K. S.; Chin, M.; Curci, G.; Diehl, T.; Easter, R. C.; Ghan, S. J.; Gong, S. L.; Hodzic, A.; Hoyle, C. R.; Iversen, T.; Jathar, S.; Jimenez, J. L.; Kaiser, J. W.; Kirkevåg, A.; Koch, D.; Kokkola, H.; Lee, Y. H.; Lin, G.; Liu, X.; Luo, G.; Ma, X.; Mann, G. W.; Mihalopoulos, N.; Morcrette, J.-J.; Müller, J.-F.; Myhre, G.; Myriokefalitakis, S.; Ng, N. L.; O'Donnell, D.; Penner, J. E.; Pozzoli, L.; Pringle, K. J.; Russell, L. M.; Schulz, M.; Sciare, J.; Seland, Ø.; Shindell, D. T.; Sillman, S.; Skeie, R. B.; Spracklen, D.; Stavrou, T.; Steenrod, S. D.; Takemura, T.; Tiitta, P.; Tilmes, S.; Tost, H.; van Noije, T.; van Zyl, P. G.; von Salzen, K.; Yu, F.; Wang, Z.; Wang, Z.; Zaveri, R. A.; Zhang, H.; Zhang, K.; Zhang, Q.; Zhang, X. The AeroCom evaluation and intercomparison of organic aerosol in global models. *Atmos. Chem. Phys.* **2014**, *14*, 10845–10895.
- (9) Scott, C. E.; Spracklen, D. V.; Pierce, J. R.; Riipinen, I.; D'Andrea, S. D.; Rap, A.; Carslaw, K. S.; Forster, P. M.; Artaxo, P.; Kulmala, M.; Rizzo, L. V.; Swietlicki, E.; Mann, G. W.; Pringle, K. J. Impact of gas-to-particle partitioning approaches on the simulated radiative effects of biogenic secondary organic aerosol. *Atmos. Chem. Phys.* **2015**, *15*, 12989–13001.
- (10) Shrivastava, M.; Cappa, C. D.; Fan, J.; Goldstein, A. H.; Guenther, A. B.; Jimenez, J. L.; Kuang, C.; Laskin, A.; Martin, S. T.; Ng, N. L.; Petäjä, T.; Pierce, J. R.; Rasch, P. J.; Roldin, P.; Seinfeld, J. H.; Shilling, J. G.; Smith, J. N.; Thornton, J. A.; Volkamer, R.; Wang, J.; Worsnop, D. R.; Zaveri, R. A.; Zelenyuk, A.; Zhang, Q. Recent advances in understanding secondary organic aerosol: Implications for global climate forcing. *Rev. Geophys.* **2017**, *55*, 509–559.
- (11) Ziemann, P. J.; Atkinson, R. Kinetics, products, and mechanisms of secondary organic aerosol formation. *Chem. Soc. Rev.* **2012**, *41*, 6582–6605.
- (12) Shiraiwa, M.; Yee, L. D.; Schilling, K. A.; Loza, C. L.; Craven, J. S.; Zuend, A.; Ziemann, P. J.; Seinfeld, J. H. Size distribution dynamics reveal particle-phase chemistry in organic aerosol formation. *Proc. Natl. Acad. Sci. U. S. A.* **2013**, *110* (29), 11746–11750.
- (13) Kuwata, M.; Martin, S. T. Particle size distributions following condensational growth in continuous flow aerosol reactors as derived from residence time distributions: Theoretical development and application to secondary organic aerosol. *Aerosol Sci. Technol.* **2012**, *46*, 937–949.
- (14) Zaveri, R. A.; Easter, R. C.; Shilling, J. E.; Seinfeld, J. H. Modeling kinetic partitioning of secondary organic aerosol and size distribution dynamics: representing effects of volatility, phase state, and particle-phase reaction. *Atmos. Chem. Phys.* **2014**, *14*, 5153–5181.
- (15) Kalberer, M.; Paulsen, D.; Sax, M.; Steinbacher, M.; Dommen, J.; Prevot, A. S. H.; Fisseha, R.; Weingartner, E.; Frankevich, V.; Zenobi, R.; Baltensperger, U. Identification of polymers as major components of atmospheric organic aerosols. *Science* **2004**, *303*, 1659–1662.
- (16) Tolocka, M. P.; Jang, M.; Ginter, J. M.; Cox, F. J.; Kamens, R. M.; Johnston, M. V. Formation of oligomers in secondary organic aerosol. *Environ. Sci. Technol.* **2004**, *38*, 1428–1434.
- (17) Heaton, K. J.; Dreyfus, M. A.; Wang, S.; Johnston, M. V. Oligomers in the early stage of biogenic secondary organic aerosol formation and growth. *Environ. Sci. Technol.* **2007**, *41*, 6129–6136.
- (18) Nguyen, T. B.; Laskin, J.; Laskin, A.; Nizkorodov, S. A. Nitrogen-containing organic compounds and oligomers in secondary organic aerosol formed by photooxidation of isoprene. *Environ. Sci. Technol.* **2011**, *45* (16), 6908–6918.
- (19) Kidd, C.; Perraud, V.; Wingen, L. M.; Finlayson-Pitts, B. J. Integrating phase and composition of secondary organic aerosol from the ozonolysis of  $\alpha$ -pinene. *Proc. Natl. Acad. Sci. U. S. A.* **2014**, *111* (21), 7552–7557.
- (20) Hawkins, L. N.; Baril, M. J.; Sedehi, N.; Galloway, M. M.; De Haan, D. O.; Schill, G. P.; Tolbert, M. A. Formation of semisolid, oligomerized aqueous SOA: Lab simulations of cloud processing. *Environ. Sci. Technol.* **2014**, *48*, 2273–2280.
- (21) Virtanen, A.; Joutsensaari, J.; Koop, T.; Kannosto, J.; Yli-Pirilä, P.; Leskinen, J.; Mäkelä, J. M.; Holopainen, J. K.; Pöschl, U.; Kulmala, M.; Worsnop, D. R.; Laaksonen, A. An amorphous solid state of biogenic secondary organic aerosol particles. *Nature* **2010**, *467*, 824–827.
- (22) Saukko, E.; Lambe, A. T.; Massoli, P.; Koop, T.; Wright, J. P.; Croasdale, D. R.; Pedernera, D. A.; Onasch, T. B.; Laaksonen, A.; Davidovits, P.; Worsnop, D. R.; Virtanen, A. Humidity-dependent phase state of SOA particles from biogenic and anthropogenic precursors. *Atmos. Chem. Phys.* **2012**, *12*, 7517–7529.
- (23) Renbaum-Wolff, L.; Grayson, J. W.; Bateman, A. P.; Kuwata, M.; Sellier, M.; Murray, B. J.; Shilling, J. E.; Martin, S. T.; Bertram, A. K. Viscosity of  $\alpha$ -pinene secondary organic material and implications for particle growth and reactivity. *Proc. Natl. Acad. Sci. U. S. A.* **2013**, *110* (20), 8014–8019.
- (24) Bateman, A. P.; Bertram, A. K.; Martin, S. T. Hygroscopic influence on the semisolid-to-liquid transition of secondary organic materials. *J. Phys. Chem. A* **2015**, *119* (19), 4386–4395.
- (25) Song, M.; Liu, P. F.; Hanna, S. J.; Martin, S. T.; Bertram, A. K. Relative humidity-dependent viscosities of isoprene-derived secondary organic material and atmospheric implications for isoprene-dominant forests. *Atmos. Chem. Phys.* **2015**, *15*, 5145–5159.
- (26) Song, M.; Liu, P. F.; Hanna, S. J.; Zaveri, R. A.; Potter, K.; You, Y.; Martin, S. T.; Bertram, A. K. Relative humidity-dependent viscosity of secondary organic material from toluene photo-oxidation and possible implications for organic particulate matter over megacities. *Atmos. Chem. Phys.* **2016**, *16*, 8817–8830.
- (27) Bateman, A. P.; Gong, Z.; Liu, P.; Sato, B.; Cirino, G.; Zhang, Y.; Artaxo, P.; Bertram, A. K.; Manzi, A. O.; Rizzo, L. V.; Souza, R. A. F.; Zaveri, R. A.; Martin, S. T. Sub-micrometre particulate matter is primarily in liquid form over Amazon rainforest. *Nat. Geosci.* **2016**, *9*, 34–37.
- (28) Vaden, T. D.; Imre, D.; Beránek, J.; Shrivastava, M.; Zelenyuk, A. Evaporation kinetics and phase of laboratory and ambient secondary organic aerosol. *Proc. Natl. Acad. Sci. U. S. A.* **2011**, *108* (6), 2190–2195.
- (29) Cappa, C. D.; Wilson, K. R. Evolution of organic aerosol mass spectra upon heating: implications for OA phase and partitioning behavior. *Atmos. Chem. Phys.* **2011**, *11*, 1895–1911.
- (30) Abramson, E.; Imre, D.; Beránek, J.; Wilson, J.; Zelenyuk, A. Experimental determination of chemical diffusion within secondary organic aerosol particles. *Phys. Chem. Chem. Phys.* **2013**, *15* (8), 2983–2991.
- (31) Zhao, Y.; Wingen, L. M.; Perraud, V.; Finlayson-Pitts, B. J. Phase, composition, and growth mechanism for secondary organic aerosol from the ozonolysis of  $\alpha$ -cedrene. *Atmos. Chem. Phys.* **2016**, *16*, 3245–3264.

- (32) Shiraiwa, M.; Seinfeld, J. H. Equilibration timescale of atmospheric secondary organic aerosol partitioning. *Geophys. Res. Lett.* **2012**, *39*, L24801.
- (33) Shiraiwa, M.; Zuend, A.; Bertram, A. K.; Seinfeld, J. H. Gas-particle partitioning of atmospheric aerosols: interplay of physical state, non-ideal mixing and morphology. *Phys. Chem. Chem. Phys.* **2013**, *15*, 11441–11453.
- (34) Shiraiwa, M.; Ammann, M.; Koop, T.; Pöschl, U. Gas uptake and chemical aging of semisolid organic aerosol particles. *Proc. Natl. Acad. Sci. U. S. A.* **2011**, *108* (27), 11003–11008.
- (35) Kuwata, M.; Martin, S. T. Phase of atmospheric secondary organic material affects its reactivity. *Proc. Natl. Acad. Sci. U. S. A.* **2012**, *109*, 17354–17359.
- (36) Li, Y. J.; Liu, P.; Gong, Z.; Wang, Y.; Bateman, A. P.; Bergoend, C.; Bertram, A. K.; Martin, S. T. Chemical reactivity and liquid/nonliquid states of secondary organic material. *Environ. Sci. Technol.* **2015**, *49* (22), 13264–13274.
- (37) Bell, D. M.; Imre, D.; Martin, S. T.; Zelenyuk, A. The properties and behavior of  $\alpha$ -pinene secondary organic aerosol particles exposed to ammonia under dry conditions. *Phys. Chem. Chem. Phys.* **2017**, *19*, 6497–6507.
- (38) Wilson, J.; Imre, D.; Beránek, J.; Shrivastava, M.; Zelenyuk, A. Evaporation kinetics of laboratory-generated secondary organic aerosols at elevated relative humidity. *Environ. Sci. Technol.* **2015**, *49* (1), 243–249.
- (39) Liu, P.; Li, Y. J.; Wang, Y.; Gilles, M. K.; Zaveri, R. A.; Bertram, A. K.; Martin, S. T. Lability of secondary organic particulate matter. *Proc. Natl. Acad. Sci. U. S. A.* **2016**, *113* (45), 12643–12648.
- (40) Yli-Juuti, T.; Pajunaja, A.; Tikkanen, O.; Buchholz, A.; Faiola, C.; Väisänen, O.; Hao, L.; Kari, E.; Peräkylä, P.; Garmash, O.; Shiraiwa, M.; Ehn, M.; Lehtinen, K.; Virtanen, A. Factors controlling the evaporation of secondary organic aerosol from  $\alpha$ -pinene ozonolysis. *Geophys. Res. Lett.* **2017**, *44*, 2562–2570.
- (41) Ye, Q.; Robinson, E. S.; Ding, X.; Ye, P.; Sullivan, R. C.; Donahue, N. M. Mixing of secondary organic aerosols versus relative humidity. *Proc. Natl. Acad. Sci. U. S. A.* **2016**, *113*, 12649–12654.
- (42) Guenther, A. B.; Jiang, X.; Heald, C. L.; Sakulyanontvittaya, T.; Duhl, T.; Emmons, L. K.; Wang, X. The Model of Emissions of Gases and Aerosols from Nature version 2.1 (MEGAN2.1): an extended and updated framework for modeling biogenic emissions. *Geosci. Model Dev.* **2012**, *5*, 1471–1492.
- (43) Liu, S.; Shilling, J. E.; Song, C.; Hiranuma, N.; Zaveri, R. A.; Russell, L. M. Hydrolysis of organonitrate functional groups in aerosol particles. *Aerosol Sci. Technol.* **2012**, *46* (12), 1359–1369.
- (44) Holmes, J. R.; O'Brien, R. J.; Crabtree, J. H.; Hecht, T. A.; Seinfeld, J. H. Measurement of ultraviolet radiation intensity in photochemical smog studies. *Environ. Sci. Technol.* **1973**, *7*, 519–523.
- (45) Liu, J. M.; D'Ambro, E. L.; Lee, B. H.; Lopez-Hilfiker, F. D.; Zaveri, R. A.; Rivera-Rios, J. C.; Keutsch, F. N.; Iyer, S.; Kurten, T.; Zhang, Z. F.; Gold, A.; Surratt, J. D.; Shilling, J. E.; Thornton, J. A. Efficient isoprene secondary organic aerosol formation from a Non-IEPOX pathway. *Environ. Sci. Technol.* **2016**, *50*, 9872–9880.
- (46) Lindinger, W.; Hansel, A.; Jordan, A. On-line monitoring of volatile organic compounds at pptv levels by means of proton-transfer-reaction mass spectrometry (PTR-MS) - Medical applications, food control and environmental research. *Int. J. Mass Spectrom. Ion Processes* **1998**, *173* (3), 191–241.
- (47) DeCarlo, P. F.; Kimmel, J. R.; Trimborn, A.; Northway, M. J.; Jayne, J. T.; Aiken, A. C.; Gonin, M.; Fuhrer, K.; Horvath, T.; Docherty, K. S.; Worsnop, D. R.; Jimenez, J. L. Field-Deployable, High-Resolution, Time-of-Flight Aerosol Mass Spectrometer. *Anal. Chem.* **2006**, *78* (24), 8281–8289.
- (48) Jayne, J. T.; Leard, D. C.; Zhang, X.; Davidovits, P.; Smith, K. A.; Kolb, C. E.; Worsnop, D. R. Development of an aerosol mass spectrometer for size and composition analysis of submicron particles. *Aerosol Sci. Technol.* **2000**, *33* (1–2), 49–70.
- (49) Allan, J. D.; Jimenez, J. L.; Williams, P. I.; Alfarra, M. R.; Bower, K. N.; Jayne, J. T.; Coe, H.; Worsnop, D. R. Quantitative sampling using an Aerodyne aerosol mass spectrometer 1. Techniques of data interpretation and error analysis. *J. Geophys. Res.* **2003**, *108* (D3), 4090.
- (50) Lee, B. H.; Lopez-Hilfiker, F. D.; Mohr, C.; Kurten, T.; Worsnop, D. R.; Thornton, J. A. An iodide-adduct high-resolution time-of-flight chemical-ionization mass spectrometer: application to atmospheric inorganic and organic compounds. *Environ. Sci. Technol.* **2014**, *48* (11), 6309–6317.
- (51) Lopez-Hilfiker, F. D.; Mohr, C.; Ehn, M.; Rubach, F.; Kleist, E.; Wildt, J.; Mentel, Th. F.; Lutz, A.; Hallquist, M.; Worsnop, D.; Thornton, J. A. A novel method for online analysis of gas and particle composition: description and evaluation of a Filter Inlet for Gases and AEROSols (FIGAERO). *Atmos. Meas. Tech.* **2014**, *7* (4), 983–1001.
- (52) D'Ambro, E. L.; Lee, B. H.; Liu, J.; Shilling, J. E.; Gaston, C. J.; Lopez-Hilfiker, F. D.; Schoebesberger, S.; Zaveri, R. A.; Mohr, C.; Lutz, A.; Zhang, Z.; Gold, A.; Surratt, J. D.; Rivera-Rios, J. C.; Keutsch, F. N.; Thornton, J. A. Molecular composition and volatility of isoprene photochemical oxidation secondary organic aerosol under low- and high-NO<sub>x</sub> conditions. *Atmos. Chem. Phys.* **2017**, *17*, 159–174.
- (53) Roach, P. J.; Laskin, J.; Laskin, A. Nanospray desorption electrospray ionization: an ambient method for liquid-extraction surface sampling in mass spectrometry. *Analyst* **2010**, *135*, 2233–2236.
- (54) Roach, P. J.; Laskin, J.; Laskin, A. Molecular characterization of organic aerosols using nanospray-desorption/electrospray ionization-mass spectrometry. *Anal. Chem.* **2010**, *82*, 7979–7986.
- (55) Zelenyuk, A.; Imre, D.; Wilson, J.; Zhang, Z.; Wang, J.; Mueller, K. Airborne single particle mass spectrometers (SPLAT II & miniSPLAT) and new software for data visualization and analysis in a geo-spatial context. *J. Am. Soc. Mass Spectrom.* **2015**, *26*, 257–270.
- (56) Zaveri, R. A.; Easter, R. C.; Fast, J. D.; Peters, L. K. Model for Simulating Aerosol Interactions and Chemistry (MOSAIC). *J. Geophys. Res.* **2008**, *113*, D13204.
- (57) Krechmer, J. E.; Coggon, M. M.; Massoli, P.; Nguyen, T. B.; Crounse, J. D.; Hu, W. W.; Day, D. A.; Tyndall, G. S.; Henze, D. K.; Rivera-Rios, J. C.; Nowak, J. B.; Kimmel, J. R.; Mauldin, R. L.; Stark, H.; Jayne, J. T.; Sipila, M.; Junninen, H.; Clair, J. M. S.; Zhang, X.; Feiner, P. A.; Zhang, L.; Miller, D. O.; Brune, W. H.; Keutsch, F. N.; Wennberg, P. O.; Seinfeld, J. H.; Worsnop, D. R.; Jimenez, J. L.; Canagaratna, M. R. Formation of low volatility organic compounds and secondary organic aerosol from isoprene hydroxyhydroperoxide low-NO oxidation. *Environ. Sci. Technol.* **2015**, *49*, 10330–10339.
- (58) Trump, E. R.; Donahue, N. M. Oligomer formation within secondary organic aerosols: equilibrium and dynamic considerations. *Atmos. Chem. Phys.* **2014**, *14*, 3691–3701.
- (59) Lopez-Hilfiker, F. D.; Mohr, C.; Ehn, M.; Rubach, F.; Kleist, E.; Wildt, J.; Mentel, Th. F.; Carrasquillo, A. J.; Daumit, K. E.; Hunter, J. F.; Kroll, J. H.; Worsnop, D. R.; Thornton, J. A. Phase partitioning and volatility of secondary organic aerosol components formed from  $\alpha$ -pinene ozonolysis and OH oxidation: the importance of accretion products and other low volatility compounds. *Atmos. Chem. Phys.* **2015**, *15*, 7765–7776.
- (60) Lopez-Hilfiker, F. D.; Mohr, C.; D'Ambro, E. L.; Lutz, A.; Riedel, T. P.; Gaston, C. J.; Iyer, S.; Zhang, Z.; Gold, A.; Surratt, J. D.; Lee, B. H.; Kurten, T.; Hu, W. W.; Jimenez, J.; Hallquist, M.; Thornton, J. A. Molecular composition and volatility of organic aerosol in the Southeastern U.S.: Implications for IEPOX derived SOA. *Environ. Sci. Technol.* **2016**, *50*, 2200–2209.
- (61) Gaston, C. J.; Lopez-Hilfiker, F. D.; Whybrew, L. E.; Hadley, O.; McNair, F.; Gao, H.; Jaffe, D. A.; Thornton, J. A. Online molecular characterization of fine particulate matter in Port Angeles, WA: Evidence for a major impact from residential wood smoke. *Atmos. Environ.* **2016**, *138*, 99–107.
- (62) Shiraiwa, M.; Li, Y.; Tsimpidi, A. P.; Karydis, V. A.; Berkemeier, T.; Pandis, S. N.; Lelieveld, J.; Koop, T.; Pöschl, U. Global distribution of particle phase state in atmospheric secondary organic aerosols. *Nat. Commun.* **2017**, *8*, 15002.